Soil contamination in arid environments and assessment of remediation applying surface evaporation capacitor model; a case study from the Judean Desert, Israel

Rotem Golan[1], Ittai Gavrieli[2], Roee Katzir[1], Galit Sharabi[2], Uri Nachshon[1]

5 [1]Institute of soil, water and environmental sciences, Agricultural Research Organization, Volcani Center, Rishon-Letsioz, 7505101, Israel.
[2]Geological Survey of Israel, 32 Yisha'ayahu Leibowitz St. Jerusalem, 9692100, Israel.

Correspondence to: Uri Nachshon (urina@agri.gov.il)

Abstract. Many of the globe arid areas are exposed to severe soil contamination events, due to the presence of highly pollutant

10 industries in these regions. In this work a case study from the Ashalim basin, at the Judean desert, Israel was used to examine the nature of solutes and contaminants transport in sandy terraces of an ephemeral stream that was exposed to a severe pollution event.

In order to to shed new light on contaminants distribution along the soil profile and transport mechanisms, in arid environments, three complimentary approaches were used: (1) Periodic on-site soil profile sampling, recording the annual solute transport

15 dynamics; (2) Laboratory analyses and controlled experiments in a rain simulator, to characterize solutes release and transport; and (3) Numerical simulation was used to define and understand the main associated processes.

The study highlights the stubborn nature of the pollutants in these natural setting that dictates they will remain near the soil surface, despite the presence of sporadic rain events. It was shown that a vertical circulation of the contaminates is occurring with soil wetting and drying cycles. The 'surface evaporation capacitor' concept of Or and Lehmann from 2019 was examined

20 and compared to field measurements and numerical simulations, and found to be a useful tool to predict the fate of the contaminants along the soil profile.

1 Introduction

Arid and semi-arid areas are defined as areas, beyond the polar and subpolar regions, where the ratio of annual precipitation to potential evapotranspiration is within the range of 0.05 to 0.65 (Gratzfeld, 2003). These areas, also known as deserts, cover

25 approximately 32% of Asia, 22% of Africa, 17% and 14% of North and South America, respectively, 7% of Europe, and 18% of Australia (Effat and Elbeih, 2020). Many of the earth deserts contain unique natural resources such as evaporative minerals (Reynolds et al., 2007), oil (Leaver, 1990), commercially important rocks such as phosphates, and limestones (Abdel-Hakeem and El-Habaak, 2021; Sharma et al., 2000) and rare minerals or elements such as diamonds and uranium (Salom and Kivinen, 2020). Consequently, and combined with low population density, low demand for agriculture lands and the low land cost, large

30   areas in the deserts are being used for industrial activities that involve highly polluting facilities. These include mines of different types (Abdel-Hakeem and El-Habaak, 2021; Effat and Elbeih, 2020; Portnov and Safriel, 2004), evaporation pans (Marazuela et al., 2020), oil production facilities (Luna et al., 2014), heavy and pollutant chemical industries (Dou et al., 2015; Effat and Elbeih, 2020; Portnov and Safriel, 2004) and landfills of different types (Cohen, 2007), including radioactive waste disposal sites (Shumway and Jackson, 2008).

35   Improper operational and management actions of these industrial activities, as well as uncontrolled and unpredicted accidents may cause severe soil, water and atmospheric contaminations. Often, such contamination events are associated with extreme climatic events such as floods (El Bastawesy and Abu El Ella, 2017; Becker et al., 2020; Gordon et al., 2018; Greenbaum, 2007; Izquierdo et al., 2020). With increasing risks for contamination events due to global climate change that includes higher probabilities of extreme rain events and floods (IPCC, 2007; Schewe et al., 2014), it is essential to better understand the

40   hydrological processes associated with such contaminations, in particular the nature of contaminants transport dynamics in arid environments and their fate thereafter. This understanding is a key for future prevention and mitigation of flood-associated contaminations in arid areas.

Natural flash flood events in arid environments occur during or following strong rain events. Water flow is typically restricted to the mainstream flow channel (MFC), whereas the elevated alluvial terraces are usually exposed to limited levels of moisture

45   (**Fig. 1A**). However, during rare and extreme rain events, which may also induce catastrophic pollution spills, the flow may reach areas beyond the MFC (**Fig. 1B**), exposing the rock slopes and terraces to unique hydrological conditions and processes. Previous studies of water infiltration processes and solute transport dynamics concentrated on the processes taking place beneath the MFC of ephemeral rivers in arid region, during and after flash floods (Amiaz et al., 2011; Basahi et al., 2018; Masoud et al., 2018). The present study focuses on governing solute transport processes that dictate the long-term fate of

50   pollutants in the sandy terraces bordering the MFC. We also present a novel use of the surface evaporation capacitor (SEC) model of Or et al. (2019), as a tool to predict the fate of solutes in the examined system and to assess the likelihood of natural soil remediation, by soil leaching with local rains. Our case study is a severe contamination event in the Ashalim Basin, an ephemeral stream in the Judean desert, described hereafter.
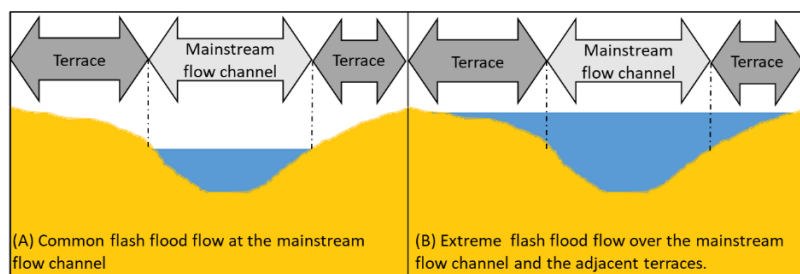
55   **Figure 1: conceptual representations of: (A) common flash flood event, where the flow is restricted to the mainstream flow channel; and (B) extreme flash flood, in which the uplands and terraces beyond the mainstream flow channel are exposed to the flood.**

1.1 The Ashalim Basin and contamination event of 2017

The Ashalim Basin, located in the Judean Desert, Israel (**Fig. 2A**), drains an area of ~80 square kilometers between Rotem
60   Plain in the west and the Dead-Sea transform depression in the east (**Fig. 2A**). At its highest point in the west the basin is
approximately 450 m above sea level, while its outlet elevation, ~15 km to the east, is about 390 m below sea level (Becker et
al., 2020; Greenbaum, 2007). In the upper, western part of the basin, the MFC curves through a 4-5 km sandy to carbonate
terrain, and is characterized by a shallow and wide stream channel, with adjacent sandy terraces to the sides, bordering the
hilly rock slopes (**Fig. 2B**). Towards the east, the landscape changes to a rocky terrain (mainly carbonates) and the stream
65   channel narrows to form a deep gorge (**Fig. 2C**). The regional climate is arid with average annual precipitation of less than
100 mm, characterized by sporadic and short rain events during winter months, in between October and March (Zoccatelli et
al., 2020). Thus, throughout most of the year the basin is dry whereas in winter flash floods may develop following strong rain
events. Annual potential evaporation is higher than 2500 mm, as measured in a meteorological station located at the south-
western edge of the basin, over a time span of nine years. The eastern part of the basin is part of the Judean Desert Nature
70   Reserve (https://en.parks.org.il/map/).

Rotem Plain, in the western part of the Ashalim basin, is the site of a complex chemical-industrial zone (**Fig. 2A**). One of the
major facilities on site is the 'Rotem-ICL' chemical plant, which produces phosphate from phosphoric rocks for the fertilizer
industry and for other phosphate-based products. A by-product of the phosphate production is phosphogypsum, which is
stockpiled in high mounds overlooking the Ashalim basin. The mounds are operational ponds used to circulate the production
75   fluids and deposit the phospogypsum. The phosphogypsum accumulates at the bottom of the ponds, thus gradually elevating
the acidic pond and forming the phosphogypsum stockpile. In June 2017, one of the dikes of the operational ponds breached,
releasing about 300,000 cubic meters of highly acidic eluents and phosphogypsum slurry into the Ashalim stream (Becker et
al., 2020; Rudnik, 2019). The acidic slurry contained also high concentrations of dissolved salts and heavy metals, derived
from the phosphoric rocks as well as from the industrial process itself. The catastrophic spill event developed into a flashflood
80   in which flow levels reached elevation significantly higher than the MFC, covering large areas of the sandy terraces and
bordering hillslopes, which commonly are not exposed to flow during flash-floods. Several years after the event the maximal
height of the acidic flow is still easily observed in the field, in the form of a bright light coloring of the surface and sediments,
in contrast to the above unaffected darker rocks and sediment (**Fig. 2B**). The pollution event caused an immediate extinction
of local fauna and flora, including the death of an entire herd of the local desert mountain goat, the Nubian Ibex *(Capra*
85   *nubiana).*
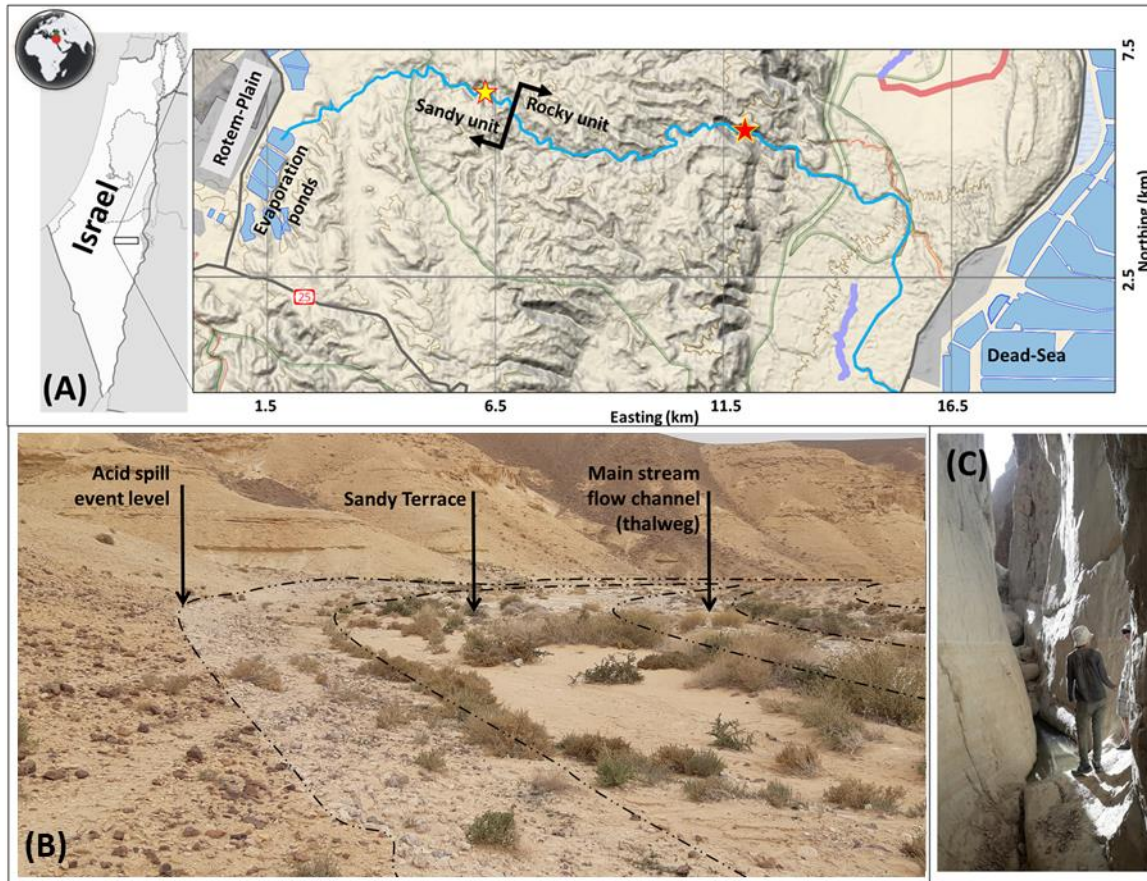
Figure 2: Location map of the Ashalim Basin and the field site (A). The light blue curve follows the main stream channel of the Ashalim Basin. Yellow and red stars designate the location of pictures (B) and (C), at the sandy unit and the deep gorge unit, respectively. Whitish coloring of surface in picture B is actual coloring due to the spill event. The picture was taken at the vicinity of field monitoring station.

1.2 Surface Evaporation Capacitor model

Or and Lehmann (2019) termed the topsoil layer that contributes water to evaporation at soil surface during first stage of evaporation (S1) as 'Surface Evaporation Capacitor' (SEC). S1 functions as such, and evaporation is maximal, as long as there is hydraulic connection between the drying front and the soil surface (Lehmann et al., 2008). The SEC model predicts if pore water at the subsurface will be flowing by capillarity towards the evaporation front and evaporates, or if it will infiltrate downwards to deeper soil levels and the groundwater, where the latter exists. Here, we use the SEC model to estimate the fate of conservative solutes and pollutants at the soil, which are being transported with the flowing pore water.

The thickness of the SEC layer that contributes water to evaporation at the soil surface is determined by the soil characteristic evaporation length, L_C (m), which combines gravity and viscous forces, and is also determined by the potential evaporation at the soil surface, E_0 (m/s), and the soil hydraulic properties (Or and Lehmann, 2019):

$$L_c = \frac{L_G}{1 + \frac{E_0}{K_{eff}}} \tag{1}$$

where K_{eff} (m/s) is the effective soil hydraulic conductivity within the SEC, and L_G (m) is the maximum length for capillary flow against gravity to sustain evaporation from the surface. L_G is determined solely by the soil physical properties, its texture and the difference in air entry pressure between the largest soil pores, h_L (m), and the smallest hydraulically connected pore, h_S (m).

$$L_G = h_S - h_L = \frac{(1-m)}{\alpha}\left(1 + \frac{1}{m}\right)^{(1+m)} \tag{2}$$

where

$$m = 1 - \frac{1}{n} \tag{3}$$

and α (1/m) and n (-) are the van Genuchten parameters which describe the connection between matric suction and soil water content, for different soil textural properties (van Genuchten, 1983).

During S1, the effective soil hydraulic conductivity (K_{eff}) is affected by the matric suction of the small pores at the soil surface, and the soil hydraulic parameters:

$$K_{eff} = 4K_S\sqrt{(1 + (\alpha \cdot h_S)^n)^{-m}}\left(1 - \left(1 - \frac{1}{1+(\alpha \cdot h_S)^n}\right)^m\right)^2 \tag{4}$$

Where K_s (m/s) is the soil hydraulic conductivity at saturation.

Determining the soil characteristic evaporation length, L_c, based upon soil properties and environmental conditions, enables to predict the flow direction of the pore water and solutes within, including contaminates, if present. In principle, following soil wetting event, a drop of water within the SEC may undergo one of the three following processes: (i) downward infiltration, to depths greater than L_C; (ii) upward flow to the soil surface, by capillarity, and evaporation at the soil surface; or (iii) no flow, provided that the SEC water content is low (~residual water content), and the hydraulic conductivity approaches zero, i.e., the pore water will not flow out of the pores. In this latter case, the water may be exposed to slow diffusive evaporation process, i.e., second stage of evaporation (S2).

For conservative solutes or pollutants that are being transported with pore water and do not interact with soil particles, the SEC model may be used to determine the fate and location of solutes accumulation. Water flow upward to the soil surface and evaporation during S1 will result in substantial accumulation of the solutes near the soil surface, and eventually may lead to salt precipitation above (efflorescence) or below (subflorescence) the soil surface (Dai et al., 2016; Nachshon et al., 2018). Water that infiltrates downward, to below the L_C will carry away the solutes and the pollutants to deeper soil levels, removing them permanently from the soil surface and the root zone. Retained pore water, at conditions of residual water content will maintain the solutes in their location while S2 evaporation will concentrate them *in situ*.

Here we combine laboratory measurements, field observations, numerical modeling and estimation of the SEC thickness at the sandy soils of the Ashalim Basin to better understand pollutants dynamics and solute transport processes at sandy soils in arid environments.

2 Materials and methods

In order to better understand solute transport processes at the sandy terraces of the contaminated Ashalim Basin, two series of experiments were conducted in the laboratory; long term monitoring of solute distribution along the soil profile was conducted

135   at the field; and a transport model was formulated, using HYDRUS-1D (Simunek et al., 2005). In addition, the SEC model was evaluated in the light of the field measurements and numerical model results.

The soil of the sandy terraces was characterized by the hydrometer method to determine soil particle size distribution (Ashworth et al., 2001), and the hanging column approach was used to define soil water retention properties (Schelle et al., 2013) and the van Genuchten parameters (van Genuchten, 1980). Hydraulic conductivity at saturation was computed by the

140   Rosetta model in HYDRUS-1D (Schaap et al., 2001). These hydrological properties, along with **Equations 1-4** and combined with field data of precipitation and evaporation, measured at a nearby meteorological station, were used to determine the thickness of the SEC layer at the sandy terraces of the Ashalim Basin. Field measurements and numerical model results were compared to and discussed in the light of the SEC model, as detailed below.

2.1 Laboratory experiments

145   Two laboratory experiments were conducted: (i) Batch leaching experiments, aimed to examine the dissolution and release dynamics of selected solutes out of the contaminated soil; and (ii) experiments in a rain simulator to study the release and transport of the solutes during rain events. For the experiments, contaminated sandy soil was collected from the contaminated terraces along the mainstream channel (yellow star in **Fig. 2A and B**). The soil samples were collected in June 2019, two years after the contamination event. Prior to any experiment or analysis in the laboratory, the collected soil was dried in an oven at

150   50°C for 48 hours, disintegrated by hand, and sieved through a 2 mm sieve.

2.1.1 Batch leaching experiments

In order to determine the composition of the major ions in the contaminated soils and the dynamics of dissolution and extraction of the substances from the soil, batch-dissolution experiments were conducted. 30 gr of the contaminated sandy soil and 30 ml of deionized water were mixed and shaken well for 10 minutes in 50 ml test tubes. The tubes were then centrifuged (3500

155   RPM) and the solutes decanted and filtered before being analyzed for their chemical composition, as detailed in **Table 1**. The solids in the test tube were then saturated again with 30 ml distilled water and the process repeated five times. The experiments were done in triplicates.

160

Table 1: Chemical analyses methods:

Parameter	Instrumentation	Error
EC, pH	Eutech PC 450, Thermo-Fisher, Waltham, MA, USA.	0.01 dS/m; 0.02 pH units
Na, K	420 Clinical Flame Photometer, Sherwood Scientific Ltd, Cambridge, UK	<10%
Ca, Mg	AAnalyst 400 Spectrometer, PerkinElmer Inc, Waltham, MA	<10%
Cl, SO$_4$, PO$_4$	Gallery Discrete Analyzer, Thermo-Fisher, Waltham, MA, USA	<%5

2.1.2 Rain simulator experiments

The rain simulation experiments aimed to shed light on dissolution and transport processes of the solutes during rain events. The experiments were conducted in a Morin-type rainfall simulator, which enables to simulate rainstorms with different rainfall intensities on inclined surfaces (Morin et al., 1967). The simulated rain events were of a 43.0 mm cumulative rain, with rain intensity of 48.0 mm/h. The rainwater used for the simulations were deionized water, to closely mimic natural rainwater. For the experiments, the examined sandy soil samples were packed in tin trays, 4 cm deep, 45 cm long and 30 cm wide, which were placed in the simulator at a slope of 9%, with four replicates. Rain experiments were conducted for three setups: (i) the contaminated sand samples as collected from the field; (ii) the contaminated sand samples from the first rain experiment after being dried in the trays in free air for two weeks; and (iii) Control sand samples collected from a nearby stream which was not exposed to the contamination event, tributary of Gmalim stream, located ~1 km north of the Ashalim Basin.

The rain simulator allows the collection of water infiltrating through the soil, as well as surface water. Infiltrating water samples were collected every few seconds at the beginning of each simulated rain event and every few minutes in the later stages of the experiments. Surface water, which had lower volumes compared to the infiltrating water were collected in ~20 minutes intervals. Water samples were analyzed in the laboratory for the chemical concentrations of selected components (**Table 1**).

2.2 Field monitoring

Field measurements were conducted to characterize solute transport and accumulation processes at the terraces of the sandy unit. On Sept. 29th, 2020, two contaminated sandy terraces, located within the sandy unit (yellow star in **Fig. 2A; Fig. 3A**), adjacent and above to the MFC were randomly selected to be monitored for their solutes transport processes over a one-year period. The two sites were referred to as 'West plot' (31.077421ºN35.256586ºE) and 'East plot' (31.077722ºN35.258020ºE). At each location soil profiling, down to a depth of ~50 cm, was done every few months. In addition, during winter, soil profiles were collected following each rain event. The collected samples were oven dried for 48 hours at 50°C, hand crushed, sieved, and mixed with deionized water at 1:1 ratio, and shook for two hours. Then chemical composition of the extracted water was

determined (**Table 1**). Daily rain depth data was available from the Israeli Nature and Parks Authority, that measured rain depth at a station located ~1 km northeast of the selected terraces.
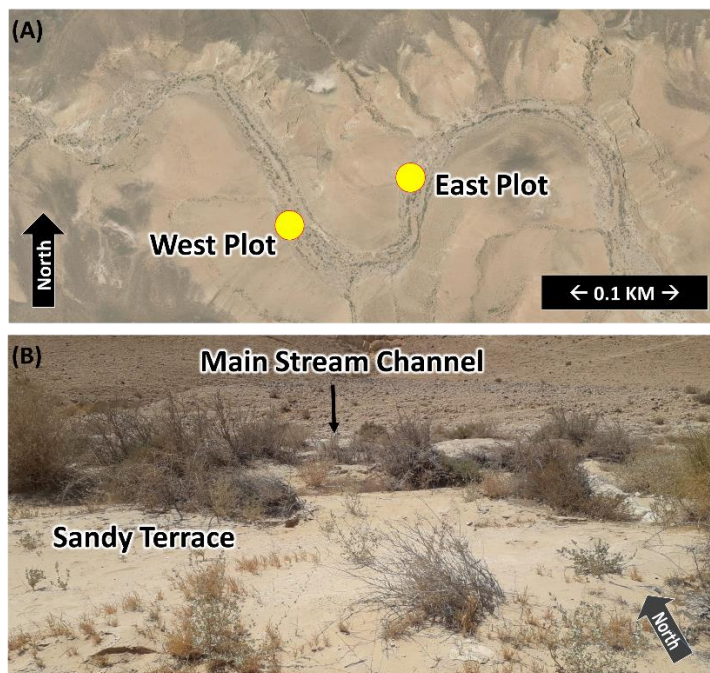
Figure 3: Aerial location map view of the 'west' (31.077421ºN35.256586ºE) and 'east' (31.077722ºN35.258020ºE)
190 **monitoring plots (A); and characteristic view of a sandy terrace, specifically at the West Plot, in adjacent to the**
mainstream channel (B).

2.3 Numerical model

A numerical simulation in HYDRUS-1D (Simunek et al., 2005) was applied to estimate the general leaching potential of solutes in sandy soils under arid climatic conditions. For this purpose, a one dimensional model was constructed and solute
195 transport was simulated over a one-year course. The modeled domain composed of a sandy soil with hydrological parameters as determined for the collected soil samples by the hanging column and hydrometer procedures (Ashworth et al., 2001; Schelle et al., 2013). Initial conditions were set as matric suction of -100 cm throughout the entire domain, corresponding to saturation degree of residual water content. The simulated polluted layer was represented as a 10 cm top layer containing a conservative solute. The solute concentration was set with a linear distribution of 10 and 0 mmol/cm^3 at the soil surface and the lower
200 boundary of the 10 cm layer, respectively. Domain's lower boundary, at depth of 100 cm, was set as free drainage, and upper boundary was set as atmospheric boundary, with precipitation events corresponding to daily rain depths as measured at the Ashalim Basin during the winter of 2020-2021. Daily potential evaporation was set following long-term measurements conducted in the nearby meteorological station (**Table 2**). In addition, in order to study and better understand the impact of rain depth on solutes removal, similar simulations were performed with rain depths 2 and 5 fold higher than measured rains.

Table 2: Averaged daily potential evaporation over the year (data from a nearby meteorological station of the Israeli Nature and Parks Authority).

Month	1	2	3	4	5	6	7	8	9	10	11	12
Daily potential evaporation (mm)	3.2	4.2	5.6	8.4	10.1	11.0	10.9	9.6	8.1	6.6	4.9	3.3

3 Results and discussion

The results will be presented in the following order to allow meaningful discussion; First, the physical measurements and hydrological properties of the examined sandy soil at the Ashalim Basin will be introduced. Following, the dynamic release of solutes from the soil will be discussed upon the batch extraction experiments and the rain simulator experimental results. Next, the long-term field monitoring measurements will be presented, followed by the numerical model results and alongside with the SEC model.

3.1 Soil physical properties

As detailed above, all laboratory experiments and analyses were done for soil samples collected in the field from the sandy terraces in the Ashalim Basin. Soil texture as defined by the hydrometer method and the USDA soil texture triangle (Shirazi and Boersma, 1984) was characterized as sandy loam, corresponding to 79% sand, 1.5% silt, and 19.5% clay. **Table 3** presents hydrological properties of the soil, as measured by the hanging column method and predicted hydraulic conductivity by the Rosetta model, for the given soil texture.

Table 3: Hydraulic properties of the examined sandy loam soil.

Property	Value
Residual water content, θ_r [-]	0.061
Saturation water content, θ_s [-]	0.36
van Genuchten α [1/cm]	0.011
van Genuchten n [-]	2.8
Saturated hydraulic conductivity, K_s [cm/d]	25.46

3.2 Solutes release

As detailed above, solutes release was examined experimentally by the batch and rain simulator experiments. Both tests pointed on similar dynamics of salts and minerals dissolution and solutes release, as detailed below.

3.2.1 Batch experiments

225 The dynamic extraction of solutes from the soil to the water, as measured in the five cycles of wetting and extraction of the batch experiment, is presented in **Fig. 4**. Over the five cycles of leaching EC dropped from average value of ~2.9 dS/m to ~2.2 dS/m (**Fig. 4A**). Concurrently, Na, Cl, K, and Mg concentrations were largely depleted by the five cycles of extraction, with most of the depletion occurring during the first two cycles. The observed rapid extraction of these solutes from the soil indicates that they most likely originated from salts with relatively high solubility, such as NaCl, Na_2SO_4, KCl, and $MgSO_4$. In addition,

230 their relatively low initial concentrations are indicative of lower quantities of these salts in the soil itself. In contrast, Ca, and SO_4 maintained relatively constant concentration levels over the five cycles of extraction, with close to 1:1 stoichiometric relation pointing on gypsum ($CaSO_4 \cdot 2H_2O$) as the likely source mineral, in line with one of the main components in the Ashalim pollution event (phosphogypsum). All extracts are saturated with respect to gypsum (SI $= 0.02$, calculated by Phreeqc Interactive 3.7.3, using phreeqc database (Parkhurst and Appelo, 2013)). Noteworthy is that their dominance in the solution

235 determines the overall salinity as expressed by the stabilizing EC.

A slight decline in SO_4 concentration is seen between cycles #1 and #2 (from ~33 to ~30 meq/l), while Ca concentrations remain relatively stable, at ~34 meq/l. This decline could point to the presence of minor amounts of relatively highly soluble sulfate minerals such as sodium sulfate and magnesium sulfate. The slight excess of Ca over SO_4 in the remaining cycles is likely due to dissolution of residual carbonate minerals, which are present in the local sands.
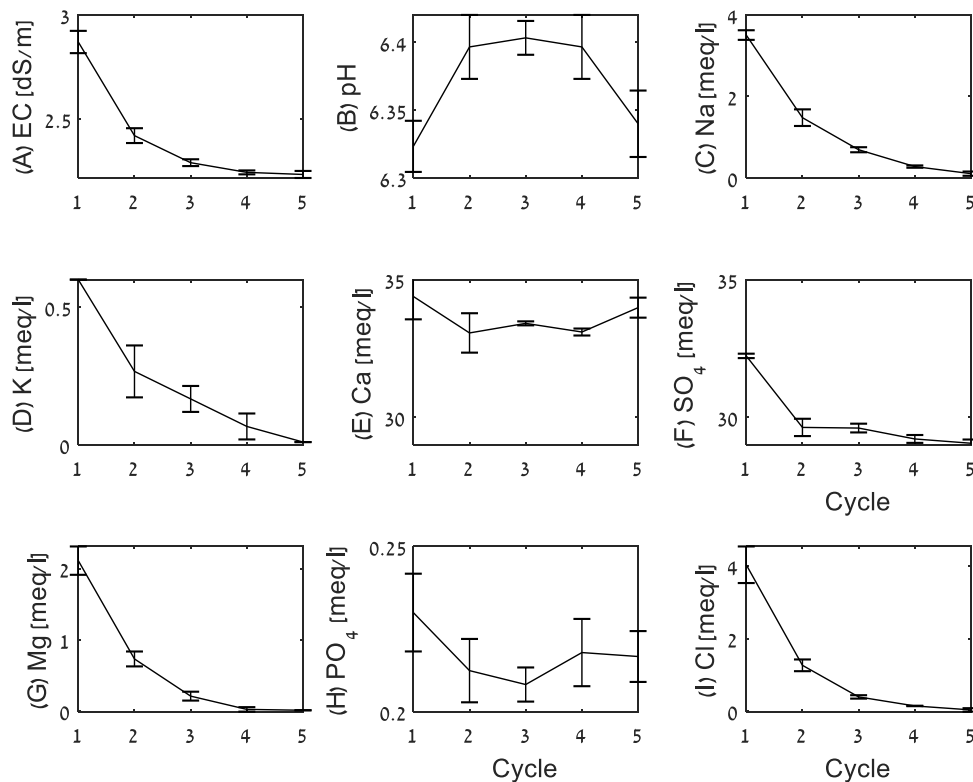
240

Figure 4: Chemical properties of leachate water from the five cycles of batch experiments. Error bars are from the triplicates.

3.2.2 Rain simulator experiments

245 More than 95% of rainwater percolated through the soil, and less than five percent of the rainwater drained along the inclined sandy slopes as runoff (**Fig. 5**). This means that for the examined conditions, the potential of lateral transport of salts and other contaminates by surface water is limited as most of the rainwater infiltrates downward through the soil.
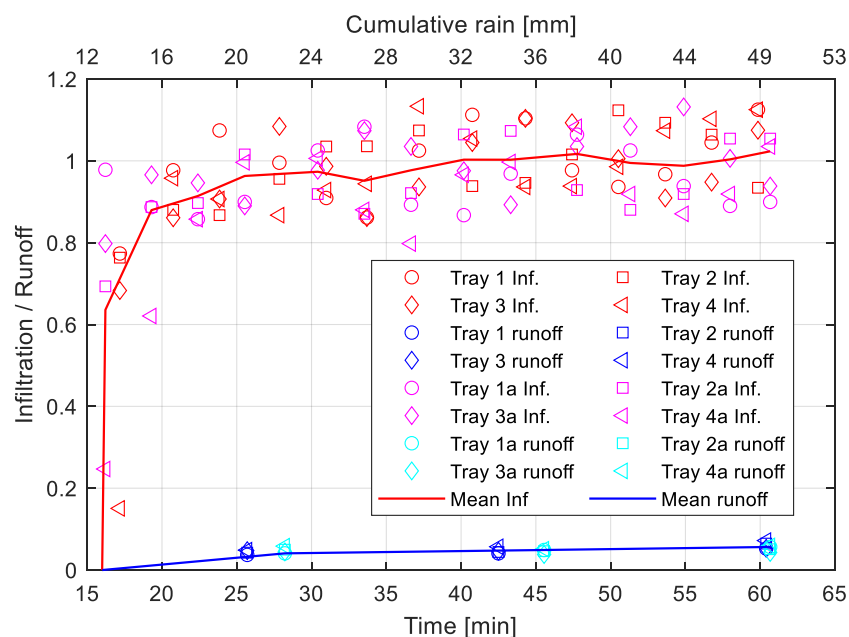
Figure 5: fractions of rainwater volume infiltrated through the soil layers and surface runoff water, as measured at the
250 **rain simulator experiments. Red and pink symbols indicate fraction of infiltrated water; the blue and aqua symbols indicate surface runoff waters. All measurements of the four repetitions (Trays) and the two simulated rain events are marked as detailed by the legend.**

The patterns of solutes release observed in the batch experiments were also found in the rain simulator experiments, in which
255 the concentrations of Na, Cl, Ca, and SO_4 were measured in samples from surface runoff and leachate water that infiltrated

through the soil (**Fig. 6**). The initial Na and Cl concentrations in the infiltrating water samples were at the order of ~40 meq/l,

with the concentrations quickly dropping off. The most likely source for these solutes is the highly soluble halite (NaCl). These

initial concentrations are much higher than those measured in the batch experiments since the water to soil ratio in the batch

experiments (1:1) was higher than the ratio of the first leachate water collected from the simulated rain events. The water to
260 soil ratio of the leachate water in the rain simulator experiment was estimated by dividing the cumulative mass of collected

water at the first reading of Na and Cl concentrations (15 mm rain depth), by the mass of soil through which the water

percolated. The mass of soil was computed for a 4 cm soil thickness, with estimated density of 1.7 g/cm^3, yielding a water to

soil ratio of only ~1:7, which explains the elevated Na and Cl concentrations in this first leachate water sample.

In agreement with the batch extraction results, Na and Cl concentrations in the leachate water rapidly declined during the
265 simulated rain event and after a cumulative rain of ~30 mm, both ions concentrations were reduced to levels of about 2 meq/l,

similar to the control (**Fig. 6A and 6B**). These concentrations drop indicate a fast and efficient dissolution process and transport

of the dissolved Na and Cl ions downward with the infiltrating water. In line with that, in the consecutive simulated rain event,

the initial concentrations of Na and Cl were relatively low, on the order of 5-10 meq/l, indicating that the reservoir of this salt

in the washed soil layer was effectively lowered compared to the initial conditions of the first simulation. However, the Na
270 and Cl concentrations at the beginning of the second rain simulation are higher than the concentrations measured at the end of

the first rain event. This is likely related to accumulation of salts near the soil surface during the drying and evaporation period between the two simulated rain events, a result of capillary water flow towards the evaporation front at the soil surface. This process enforced the accumulation and precipitation of NaCl at the soil surface. Consequently, the water infiltrated through the soil at the beginning of the second rain event dissolved the cumulated salt and pushed the solutes downward, at relatively

275 high concentration. Similarly to the first rain event, after cumulative rain of ~20 mm, both Na and Cl concentrations in both the infiltrated and runoff waters were reduced to negligible levels, of less than 2 meq/l.

Ca and SO$_4$, on the other hand, which are associated to the phosphogypsum that is less soluble than halite, and is the major mineral that was deposited during the pollution event, maintained high concentration levels in the infiltrating water, on the order of 40 meq/l, during both cycles of simulated rain events, much higher than those measured concentrations at the control.

280 As aforementioned, these high and relatively stable concentration levels are indicative of the high reservoir of phosphogypsum in the polluted sand, effectively acting as a slow release source for both ions. In concur with the batch experiment results, and for the same reasons, the Ca concentrations were more stable than the SO$_4$ concentrations which exhibited some decline with time (from ~40 to ~30 meq/l).

As detailed above, due to rapid processes of NaCl dissolution and transport of the ions downward, minor concentrations of Na

285 and Cl were measured at the surface runoff water, in the two simulated rain events (**Fig. 6A and 6B**). On the other hand, Ca and SO$_4$ concentrations in the runoff water from the first simulated rain event were high and similar to those measured in the infiltrating water. This indicates the presence of sufficient amount of gypsum at the soil surface to interact and dissolve in the surface water. However, in the second simulated rain event, both Ca and SO$_4$ concentrations at the surface runoff water were lower, probably due to substantial dissolution and removal of the gypsum from the very top levels of the soil profile during

290 the first rain event.

Given the above detailed experimental results and observations, a similar process is expected under natural conditions, whereby the contaminates and solutes from the upper soil will be mobilized by the infiltrating rain water to the lower and deeper parts of the soil profile. This process was further studied in the field and by the numerical modelling.
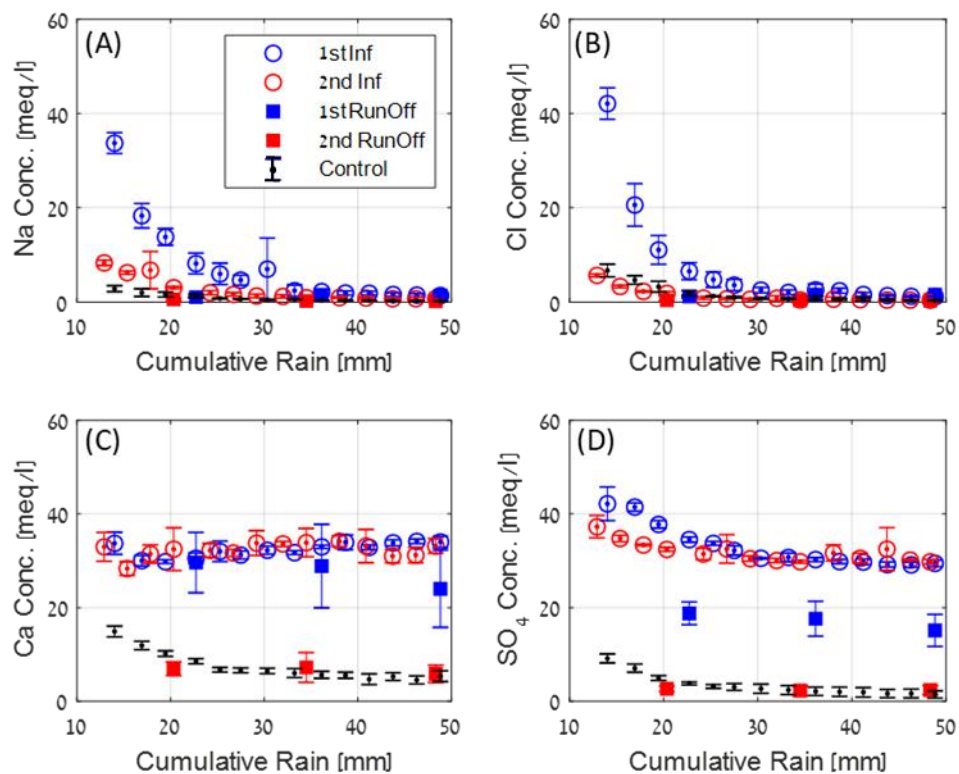
Figure 6: Measured concentrations of Na (A), Cl (B), Ca (C), and SO₄ (D) of runoff water (squares) and infiltrated water (open circles) during two consecutive simulated rain events. Blue and red symbols are for first and second simulated rain events, respectively. Black symbols represent the un-contaminated control soil. Error bars are from the four replicas.

3.3 Field measurements - annual salt dynamic in sandy alluvial terraces

Temporal monitoring of the soil profiles in two sandy alluvial terraces was carried between the summers of 2020 and 2021. Major ions compositions along the soil profiles were characterized, for extracted soil water (1:1 ratio), as detailed above. The Ca and Cl measurements are hereafter presented and discussed, as these originate from two different salts, with markedly different solubilities and sources, namely halite and phosphogypsum. In addition, Cl is a conservative anion that do not interacts with the soil, while the Ca cation may be absorbed to clay particles.

Figure 7 present the results from the field measurements. On an annual scale, no change was found in Cl and Ca concentrations at the soil surface of the eastern plot between September 2020 and September 2021. Cl concentrations were on the order of 1.5 meq/l (**Fig. 7A-B**), and Ca concentrations were on the order of 37 meq/l (**Fig. 7C-D**). The difference in concentrations between Cl and Ca are in accordance with the laboratory experiments, reflecting the abundance of gypsum in the contaminated soils. In the western plot, no changes in Cl concentrations at the soil surface were observed between September 2020 and September 2021 (**Fig. 7E-F**). However, Ca concentrations declined by ~20% between September 2020 to September 2021 (**Fig. 7G-H**). When examining the ions concentrations dynamics along the soil profiles in higher temporal resolution, between September

2020 and September 2021, it is evident that in both plots, during the winter months (October – March) Cl and Ca concentrations at the upper levels of the soil profiles were reduced, due to dissolution of the salts and the leaching of the solutes downward with the infiltrating rainwater. Consequently, the concentrations of the ions were elevated at the subsurface, at depths of 30-

315   40 cm, and 50-60 cm for the East plot and West plot, respectively. These observations, point to the dynamic nature of salts dissolution and solutes transport processes in the examined system. However, despite the high mobility of the solutes, under the arid conditions of the Ashalim Basin, the overall flushing and removal of the solutes and contaminants to significant depths is negligible. Apparently, the winter infiltration and leaching processes are not sufficient to mobilize the solutes deep enough to prevent their rise back by capillarity, during the long summer months, to the evaporation front at the soil surface.

320   As detailed above, the SEC model may be used to assess the effective depth from which contaminated pore water will not return by capillarity to the soil surface. The thickness of the SEC layer was calculated for the field site based on its hydrological properties (**Table 3**) and climatic conditions (**Fig. 7 I-J**). The lower boundary of the SEC layer is depicted in **Fig. 7** by the red contours but its depth changes over the year due to temporal changes in the potential evaporation, E_0. In the eastern plot, the winter downward leaching of both Ca and Cl solutes did not pass the lower boundary of the SEC (**Fig. 7A, C**). Consequently,

325   during the dry summer months, from April onward, pore water and associated dissolved solutes were available for upward capillary flow towards the soil surface, where evaporation takes place. At the evaporation front, the solutes become concentrated in the solution and salts and minerals precipitate to form solid crusts at the soil surface (**Fig. 8**).

In the West plot however, the infiltrating water mobilized some of the Cl and Ca ions to depths greater than the lower boundary of the SEC. Beyond this depth the water and ions will not return to the soil surface by capillary flow. This may explain the

330   20% reduction in Ca concentration at the soil surface of the West plot in summer 2021 as compared to summer 2020 (**Fig. 7H**). In contrast to the Ca concentrations, the Cl soil surface concentrations were similar for September 2020 and September 2021. However, the center mass of the Cl contaminated zone was lowered from ~20 cm depth in summer 2020 to ~40 cm depth in summer 2021. A similar process may also take place with Ca, which may be obscured due to the higher Ca concentrations and the presence of phosphogypsum.

335   The disparities between the East and West plots could be attributed to more efficient leaching processes that occurred in the West plot, due to slight differences in local meso-topography and soil properties. The field measurements demonstrate the dynamic nature of the solutes as they move vertically along the soil profile with wetting and drying events. In accordance with the SEC model, as long as the solutes are not mobilized below the lower boundary of the SEC layer, they are expected to migrate upward during the dry summer months towards the evaporation front at the soil surface. Presently (2024), more than

340   six years since the contamination event, salt crusts, mainly of phosphogypsum, are widely seen in the contaminated basin (**Fig. 8**). For additional evaluation and understanding of water flow processes and solute transport dynamics, a numerical model was used to examine the system, as detailed below.
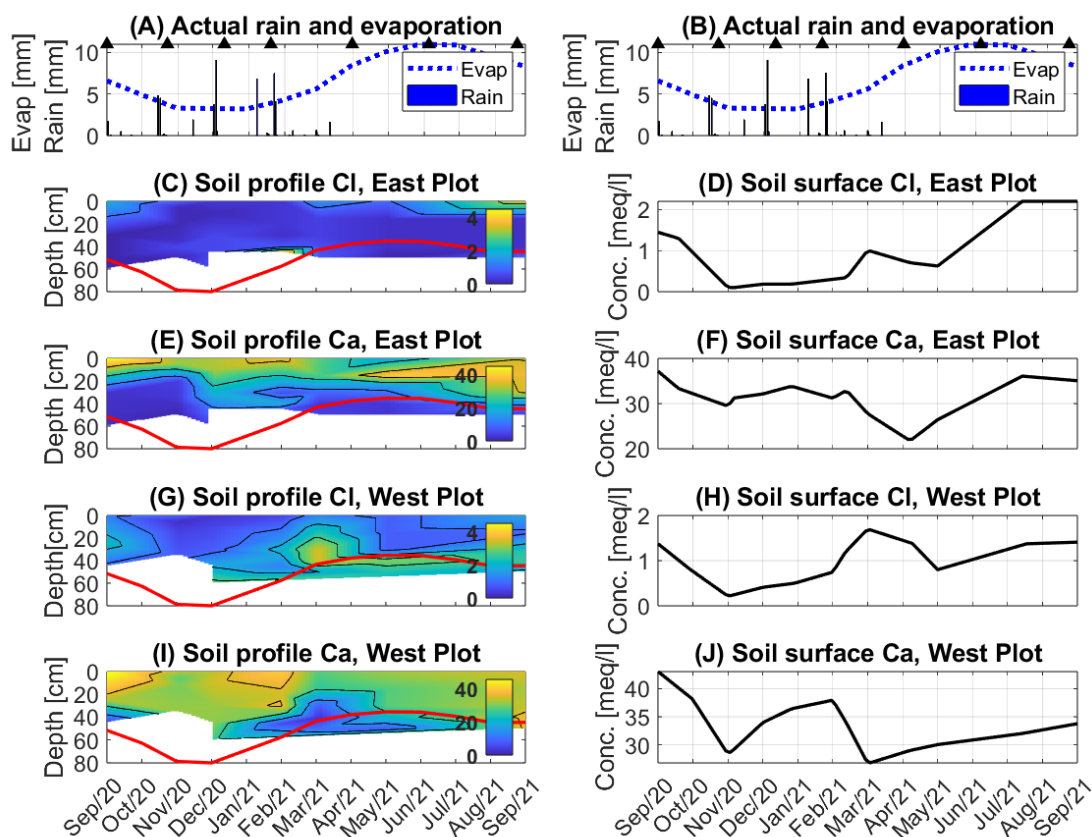
Figure 7: Temporal changes in Ca and Cl depth profiles in the sandy terraces, as measured at the East (A-D) and West
345 **Plots (E-H). The left panels present Cl and Ca concentrations (meq/l) over the entire soil profiles, down to the maximal depth that was sampled. The red contours mark the lower boundary of the SEC layer. The right panels present ions concentrations at the soil surface only. Precipitation and evaporation are presented in (I-J). Triangles indicate time of soil sampling.**

350 **Figure 8: Thin and brittle crust of gypsum that formed over the contaminated sandy soils.**

3.4 Numerical simulation model

The numerical model presents solute concentration levels (**Fig. 9C, E, G**), and water flow directions and velocities (**Fig. 9D, F, H**) along a 100 cm soil profile over a time period of 12 months. Precipitation and evaporation conditions measured at the field site between September 2020 and September 2021 (**Fig. 9A-B**) were used to define the upper boundary condition for the reference simulation. Additional two simulations were done for increased precipitation by two and five folds.

355

Model results for the actual rain and evaporation conditions demonstrate that the removal of solutes to depths greater than 30 cm is negligible. It is seen in **Fig. 9C** that for the examined setup and typical climatic conditions, the solutes are being leached downward during and following rain events, whereas in the following dry periods they are being transported upward by rising capillary water towards the evaporation front at the soil surface. Therefore, and in agreement with field measurements, over a winter-summer cycle, the high concentration of the solutes at the upper levels of the soil profile is maintained also in the simulation. **Figure 9D** presents water flow directions and velocities along the soil profile, where negative values (bluish colours) indicate downward infiltration, and positive values (yellowish colours) indicate upward capillary flow. It is seen that for the prevailing climatic conditions, only three rain events resulted in a notable downward transport of the solutes to depths of about 20 cm, and instantaneously after the rain events ended, water flow directions were reversed (**Fig. 9D**). This is in accordance with field measurements and the SEC model, with its lower boundary marked by the red contours in **Fig. 9**. As aforementioned, solutes that do not leach to depths greater than this SEC lower boundary are available for upward capillary flow towards the evaporation front, at the soil surface.

360

365

In the simulated conditions of doubled rain depth, during the two rain events (December 2020, and February 2021) the maximal depth of infiltrating water approaches the lower boundary of the SEC layer (**Fig. 9F**), and consequently, a minor reduction in solutes concentration at the upper levels of the soil profile is simulated. For the extreme simulated conditions of five times greater rain depth than natural conditions, the depth of the infiltrating water is much deeper than the SEC depth (**Fig. 9H**), and indeed the upper levels of the soil profile are completely depleted of the solutes (**Fig. 9G**).

370
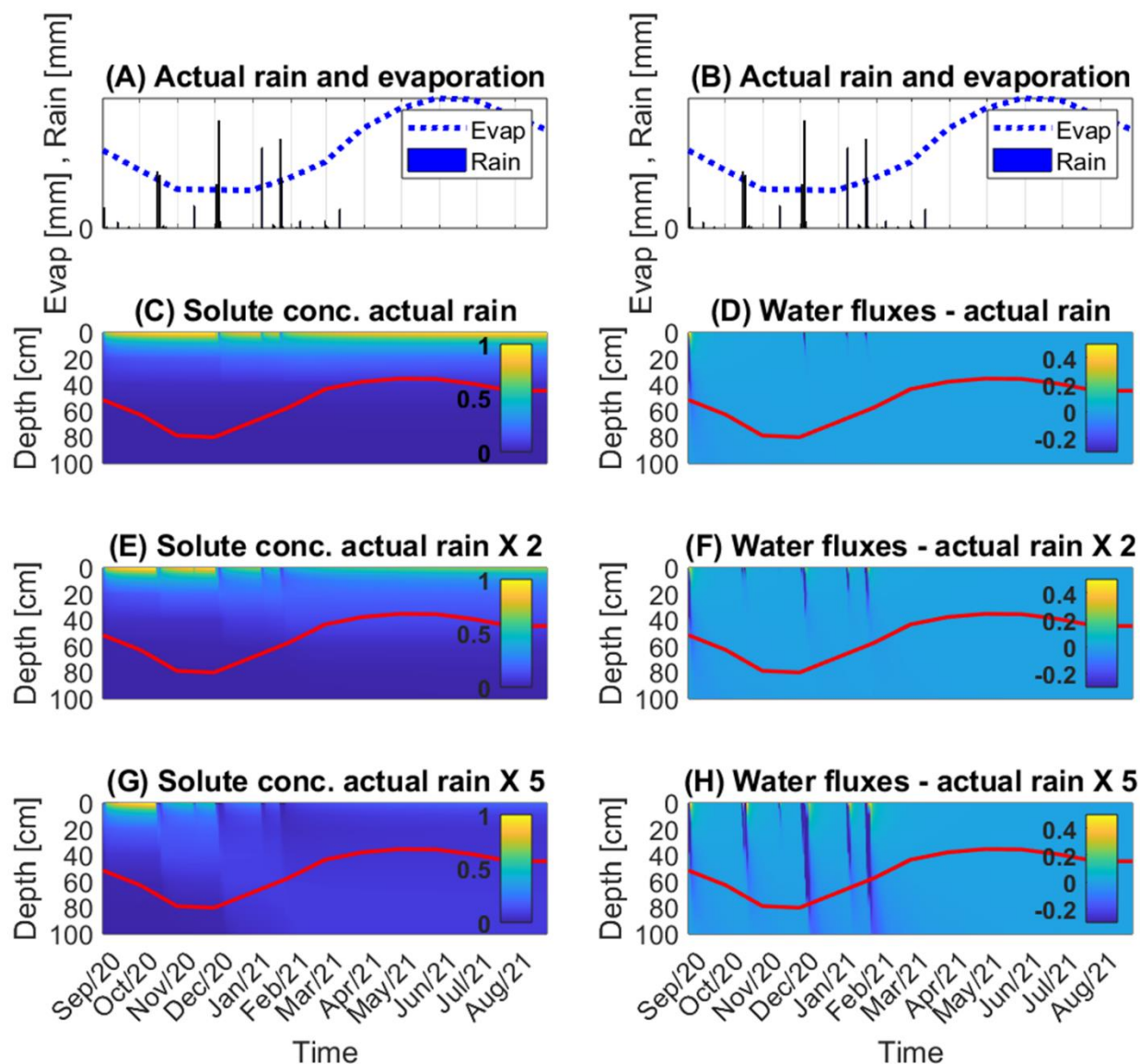
Figure 9: Numerical simulation results for solute concentration (left panels) and water fluxes (right panels) for three precipitation scenarios. (A) and (B) present the measured precipitation and potential evaporation conditions used for the simulation. (C, D) present computed solute concentration and water flow velocities, respectively, for actual climatic conditions. (E, F), and (G, H), present the same properties, for two and five folds elevated precipitation, respectively. Positive values in (B, D, F, H) indicate upward water flow. Red line signifies the calculated characteristic evaporation length of the soil, L_C, which is the lower boundary of the SEC.

4 Summary and conclusions

Experimental results, field measurements, and numerical model simulations all indicate that under arid conditions and environments, the mobilization and removal of solutes and pollutants to substantial depths in sandy soils is a minor process

even when considering solutes that do not tend to be absorbed to soil particles. Given the relatively high hydraulic conductivities of the sandy soils it is apparent that similar conclusions can be drawn for heavier and less permeable soils under arid conditions. The sporadic rain events that occur in arid environments enable only minor downward mobilization of the solutes, whereas the dry periods between such rain events are sufficient to force capillary upward transport of the solutes and dissolved pollutants. **Figure 10** is a conceptual model that illustrates the dynamics of water flow and solute transport processes, as demonstrated in this work. The soil evaporation capacitor model (Or and Lehmann, 2019) which describes the depth of soil that contributes water for the first stage of evaporation, was applied to estimate the depth to which the solutes and contaminates circulate vertically, further supporting the conceptual model.
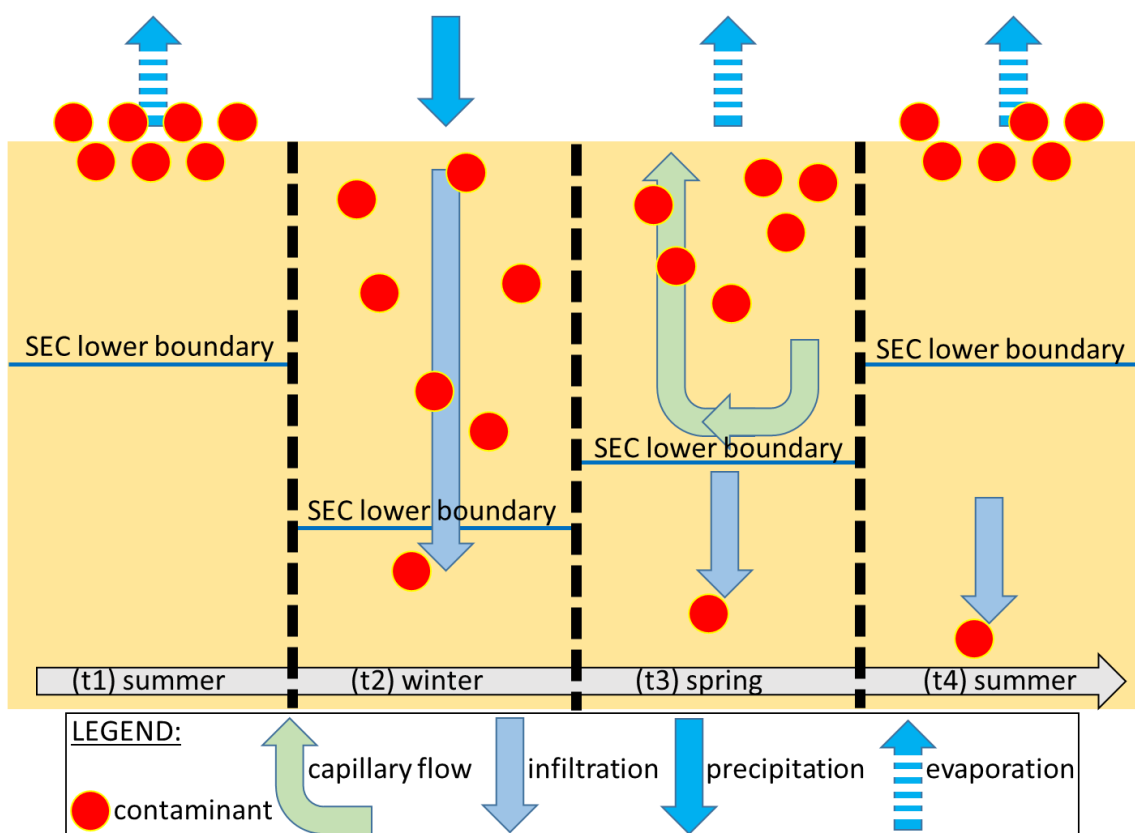
Figure 10: Conceptual model describing the fate of solutes along a soil profile under arid environments following the SEC concept. During rain events the solutes are being leached downward, but as long as they remain within the SEC zone, they can move upward with capillary water, towards the evaporation front at the soil surface. Solutes that are mobilized to depths greater than the SEC lower boundary can no longer flow upward towards the soil surface.

Since catastrophic pollution events in arid environments are in many cases of extreme magnitude, and related to extreme flash flood events, it is likely that vast areas beyond the MFC will be exposed to the contamination. These areas, however, do not see regular and natural flash floods, and thus natural attenuation processes driven by water are expected to be very limited in their ability to suffice long-term remediation. Consequently, natural attenuation potential of these areas is very limited and

slow. Therefore, it is estimated that the terraces will remain polluted long after the spill event, imposing significant chemical stress to the habitat and rendering it to slow remediation. During this period, they may also act as a slow release source of contamination to the environment.

405 **Competing interests**

The contact author has declared that none of the authors has any competing interests

References

Abdel-Hakeem, M. and El-Habaak, G.: The potential production of rock-based fertilizer and soil conditioner from phosphate mine wastes: A case study from Abu-Tartur plateau in the Western Desert of Egypt, J. Clean. Prod., 329, 129761, 410 doi:10.1016/j.jclepro.2021.129761, 2021.

Amiaz, Y., Sorek, S., Enzel, Y. and Dahan, O.: Solute transport in the vadose zone and groundwater during flash floods, Water Resour. Res., 47(10), doi:10.1029/2011WR010747, 2011.

Ashworth, J., Keyes, D., Kirk, R. and Lessard, R.: STANDARD PROCEDURE IN THE HYDROMETER METHOD FOR PARTICLE SIZE ANALYSIS, Commun. Soil Sci. Plant Anal., 32(5–6), 633–642, doi:10.1081/CSS-100103897, 2001.

415 Basahi, J. M., Masoud, M. H. Z. and Rajmohan, N.: Effect of flash flood on trace metal pollution in the groundwater - Wadi Baysh Basin, western Saudi Arabia, J. African Earth Sci., 147, 338–351, doi:10.1016/j.jafrearsci.2018.06.032, 2018.

El Bastawesy, M. and Abu El Ella, E. M.: Quantitative estimates of flash flood discharge into waste water disposal sites in Wadi Al Saaf, the Eastern Desert of Egypt, J. African Earth Sci., 136, 312–318, doi:10.1016/j.jafrearsci.2017.03.008, 2017.

Becker, N., Gross, Y. and Lavee, D.: Cost–benefit analysis of restoring an ephemeral desert stream after an ecological accident, 420 Water Policy, 22(3), 328–347, doi:10.2166/wp.2020.014, 2020.

Cohen, N.: Ramat Hovav industrial park in the Negev desert–Israel, Present Environ. Sustain. Dev., 1, 3–14, 2007.

Dai, S., Shin, H. and Santamarina, J. C.: Formation and development of salt crusts on soil surfaces, Acta Geotech., 11(5), 1103–1109, doi:10.1007/s11440-015-0421-9, 2016.

Dou, M., Mi, Q., Li, C. and Wang, Y.: Ecological desert environment suffers from industrial wastewater pollution in 425 northwestern China, Environ. Earth Sci., 74(4), 3681–3683, doi:10.1007/s12665-015-4438-z, 2015.

Effat, H. A. and Elbeih, S. F.: A geospatial model for allocating potential urban–industrial zones in a desert: Case study Matrouh, Egypt, Model. Earth Syst. Environ., 6(4), 2033–2046, doi:10.1007/s40808-020-00806-w, 2020.

van Genuchten, M. T.: A Closed-form Equation for Predicting the Hydraulic Conductivity of Unsaturated Soils, Soil Sci. Soc. Am. J., 44(5), 892–898, 1980.

430 van Genuchten, M. T.: Analyzing crop salt tolerance data: Model description and user's manual, Washington, DC., 1983.

Gordon, G., Stavi, I., Shavit, U. and Rosenzweig, R.: Oil spill effects on soil hydrophobicity and related properties in a hyper-arid region, Geoderma, 312, 114–120, doi:10.1016/j.geoderma.2017.10.008, 2018.

Gratzfeld, J.: Extractive industries in arid and semi-arid zones: Environmental planning and management, edited by J. Gratzfeld, IUCN., 2003.

435 Greenbaum, N.: Assessment of dam failure flood and a natural, high-magnitude flood in a hyperarid region using paleoflood hydrology, Nahal Ashalim catchment, Dead Sea, Israel, Water Resour. Res., 43(2), doi:10.1029/2006WR004956, 2007.

IPCC: Climate Change 2007: The Physical Science Basis., 2007.

Izquierdo, T., Bonnail, E., Abad, M., Dias, M. I., Prudêncio, M. I., Marques, R., Rodríguez-Vidal, J. and Ruiz, F.: Pollution and potential risk assessment of flood sediments in the urban area of the mining Copiapó basin (Atacama Desert), J. South
440 Am. Earth Sci., 103, 102714, doi:10.1016/j.jsames.2020.102714, 2020.

Leaver, R.: International oil and international regimes: Mirages in a desert, Aust. J. Int. Aff., 44(2), 143–154, doi:10.1080/10357719008445028, 1990.

Lehmann, P., Assouline, S. and Or, D.: Characteristic lengths affecting evaporative drying of porous media, Phys. Rev. E, 77(5), 056309, doi:10.1103/PhysRevE.77.056309, 2008.

445 Luna, D., Calero, J., Sancho, E. D., Luna, C., Posadillo, A., Bautista, F. M., Romero, A. A., Berbel, J. and Verdugo, C.: Technological challenges for the production of biodiesel in arid lands, J. Arid Environ., 102, 127–138, doi:10.1016/j.jaridenv.2013.11.014, 2014.

Marazuela, M. A., Vázquez-Suñé, E., Ayora, C. and García-Gil, A.: Towards more sustainable brine extraction in salt flats: Learning from the Salar de Atacama, Sci. Total Environ., 703, 135605, doi:10.1016/j.scitotenv.2019.135605, 2020.

450 Masoud, M. H. Z., Basahi, J. M. and Rajmohan, N.: Impact of flash flood recharge on groundwater quality and its suitability in the Wadi Baysh Basin, Western Saudi Arabia: an integrated approach, Environ. Earth Sci., 77(10), 395, doi:10.1007/s12665-018-7578-0, 2018.

Morin, J., Goldberg, D. and Seginer, I.: A Rainfall Simulator with a Rotating Disk, Trans. ASAE, 10(1), 0074–0077, doi:10.13031/2013.39599, 1967.

455 Nachshon, U., Weisbrod, N., Katzir, R. and Nasser, A.: NaCl Crust Architecture and Its Impact on Evaporation: Three-

Dimensional Insights, Geophys. Res. Lett., 45(12), 6100–6108, doi:10.1029/2018GL078363, 2018.

Or, D. and Lehmann, P.: Surface Evaporative Capacitance: How Soil Type and Rainfall Characteristics Affect Global-Scale Surface Evaporation, Water Resour. Res., 55(1), 519–539, doi:10.1029/2018WR024050, 2019.

Parkhurst, D. L. and Appelo, C. A. J.: Description of input and examples for PHREEQC version 3—a computer program for speciation, batch-reaction, one-dimensional transport, and inverse geochemical calculations, in US geological survey techniques and methods, vol. 6(A43), p. 497., 2013.

Portnov, B. A. and Safriel, U. N.: Combating desertification in the Negev: dryland agriculture vs. dryland urbanization, J. Arid Environ., 56(4), 659–680, doi:10.1016/S0140-1963(03)00087-9, 2004.

Reynolds, R. L., Yount, J. C., Reheis, M., Goldstein, H., Chavez, P., Fulton, R., Whitney, J., Fuller, C. and Forester, R. M.: Dust emission from wet and dry playas in the Mojave Desert, USA, Earth Surf. Process. Landforms, 32(12), 1811–1827, doi:10.1002/esp.1515, 2007.

Rudnik, G.: 2D Hydrodynamic Modelling of the 2017 Reservoir Dam Failure at Ashalim River Catchment, Dead Sea, Israel, Brandenburg University of Technology., 2019.

Salom, A. T. and Kivinen, S.: Closed and abandoned mines in Namibia: a critical review of environmental impacts and constraints to rehabilitation, South African Geogr. J., 102(3), 389–405, doi:10.1080/03736245.2019.1698450, 2020.

Schaap, M. G., Leij, F. J. and van Genuchten, M. T.: rosetta : a computer program for estimating soil hydraulic parameters with hierarchical pedotransfer functions, J. Hydrol., 251(3–4), 163–176, doi:10.1016/S0022-1694(01)00466-8, 2001.

Schelle, H., Heise, L., Jänicke, K. and Durner, W.: Water retention characteristics of soils over the whole moisture range: a comparison of laboratory methods, Eur. J. Soil Sci., 64(6), 814–821, doi:10.1111/ejss.12108, 2013.

Schewe, J., Heinke, J., Gerten, D., Haddeland, I., Arnell, N. W., Clark, D. B., Dankers, R., Eisner, S., Fekete, B. M., Colón-González, F. J., Gosling, S. N., Kim, H., Liu, X., Masaki, Y., Portmann, F. T., Satoh, Y., Stacke, T., Tang, Q., Wada, Y., Wisser, D., Albrecht, T., Frieler, K., Piontek, F., Warszawski, L. and Kabat, P.: Multimodel assessment of water scarcity under climate change., Proc. Natl. Acad. Sci. U. S. A., 111(9), 3245–3250, doi:10.1073/pnas.1222460110, 2014.

Sharma, K. D., Kumar, S. and Gough, L. P.: Rehabilitation of lands mined for limestone in the Indian desert, L. Degrad. Dev., 11(6), 563–574, doi:10.1002/1099-145X(200011/12)11:6<563::AID-LDR414>3.0.CO;2-I, 2000.

Shirazi, M. A. and Boersma, L.: A Unifying Quantitative Analysis of Soil Texture, Soil Sci. Soc. Am. J., 48(1), 142–147, doi:10.2136/sssaj1984.03615995004800010026x, 1984.

Shumway, J. M. and Jackson, R. H.: Place Making, Hazardous Waste, And The Development Of Tooele County, Utah*,

Geogr. Rev., 98(4), 433–455, doi:10.1111/j.1931-0846.2008.tb00311.x, 2008.

485 Simunek, J., Van Genuchten, M. and Sejna, M.: The HYDRUS-1D software package for simulating the one-dimensional movement of water, heat, and multiple solutes in variably-saturated media., 2005.

Zoccatelli, D., Marra, F., Smith, J., Goodrich, D., Unkrich, C., Rosensaft, M. and Morin, E.: Hydrological modelling in desert areas of the eastern Mediterranean, J. Hydrol., 587, 124879, doi:10.1016/j.jhydrol.2020.124879, 2020.

490